DOI 10.4430/bgo00393

Anisotropy estimate from vertical (V_{SV}) and horizontal (V_{SH}) components of S-wave velocity using ray-based tomography

G. Böhm, F. Accaino and F. Da Col

Istituto Nazionale di Oceanografia e di Geofisica Sperimentale - OGS, Trieste, Italy

(Received: 17 December 2021; accepted: 19 April 2022; published online: 27 July 2022)

ABSTRACT The acquisition of S-wave seismic data, separating S_H (orthogonal to the seismic line) and S_V (parallel to the seismic line) wavefields on the same seismic line, is not so frequent. However, this type of acquisition allows obtaining important information on the investigated area; in particular the anisotropy of the sediments, which can be detected from the differences between the corresponding two velocity fields. In this work, we analysed the S_V- and S_H-wave data in order to answer two questions: how can we estimate anisotropy from the comparison of the velocities of the S_V and S_H wavefields? What information can be obtained about the dip and strike angles of the anisotropic layers from this analysis? For this purpose, we used the travel time tomography to obtain the two velocity fields (V_{SV} and V_{SH}) and to exploit the computed ray paths from which we can know the directions of each ray segment crossing the model, associated with each V_S component. We, then, used them, together with the V_{SV}/V_{SH} values obtained from the tomography, to estimate the anisotropy and the orientation of the anisotropic layer, defined by the slope (dip) and the azimuth angle (strike). Furthermore, we tried to define a possible relationship between the V_{SV} and V_{SH} components with the anisotropy parameters, the direction of the rays and the geometry of the anisotropic layer.

Key words: anisotropy, S_H- S_V- waves, ray-based tomography, 3D model.

1. Introduction

In seismic exploration, it is not very common to acquire both S_V- and S_H-wave data along the same survey line. However, since the 1980s, a number of scientific papers, related to both S_V and S_H acquisitions, have been published. Most of these are aimed at hydrocarbon exploration, while only few focus on near surface problems. Macrides and Kelamis (2000) described a nine-component (9-C) shear wave experiment in central Saudi Arabia; in their report, Beecherl and Hardage (2004) present a very detailed description of the effect of the different components of shear waves obtained by a 9-C acquisition technology; Leary *et al.* (1987) highlight the differences between S_V and S_H waves in a fracture zone; Fishman and Ahmad (1995) analysed the effect of S_H, S_V and P waves in an alluvial valley. Concerning anisotropy, a few papers discussed the aspect of anisotropy with respect to the shear waves and in particular using both S_V and S_H data. Kelter and Bancoft (2004) showed several examples of S_H and S_V waves propagation in anisotropic media. Very recently, Wang and Zhang (2021) proposed a method to recover the γ parameter from a rock-physics based relation between the shear-wave impedance and the vertical S-wave velocity, from well data. Other papers estimated anisotropy from the shear-wave splitting (Bale

et al., 2009; Suroso *et al.*, 2017), particularly in a seismological context. Chmiel and Bardainne (2014) estimated the velocity model from microseismic events with P, S_V, and S_H waves using the simulated annealing method.

The differences between the S_V- and S_H- wave velocities (V_{SV} and V_{SH}) in the same investigated area are certainly a reliable indicator of the possible presence of anisotropy in the geological sequence. Furthermore, these differences, in particular their ratio (V_{SV}/V_{SH}), can be used to obtain information about the geometry of the anisotropic layers: slope and azimuth angle.

In this work, we estimate the anisotropy by using a non-conventional approach based on the geometrical relationship between the S-wave components and the plane of anisotropic layer, starting from the ray paths computed by the anisotropic ray-based travel time tomography used for the tomographic inversion of the S_V and S_H arrivals.

2. The theory and the proposed method

From the general concept of anisotropy, it is known that from the equation of motion:

$$\rho \frac{\partial^2 u_i}{\partial t^2} = \frac{\partial \tau_{ij}}{\partial x_j} \tag{1}$$

where ρ is the density, u is particle motion, τ is the stress tensor, and from the stress-strain relation:

$$\tilde{\tau} = \tilde{\tilde{C}}\tilde{E} \tag{2}$$

where $\tilde{\tau}$ is the stress tensor, $\tilde{\tilde{C}}$ is the stiffness tensor, $\tilde{E}$ is the strain tensor, according to the Hooke's law (Love, 1927), we obtain the wave equation:

$$\rho \frac{\partial^2 u_i}{\partial t^2} = C_{ijmn} \frac{\partial^2 u_m}{\partial x_n \partial x_j} \tag{3}$$

where C_{ijmn} (stiffness tensor) is a 3×3×3×3 tensor that can be rewritten into a 6×6 matrix $C_{\alpha\beta}$, through a re-mapping of the indexes [$ij \Rightarrow \alpha$ and $mn \Rightarrow \beta$: Musgrave (1970)]:

$$C_{\alpha\beta}\begin{bmatrix} C_{11} & C_{12} & C_{13} & C_{14} & C_{15} & C_{16} \\ C_{21} & C_{22} & C_{23} & C_{24} & C_{25} & C_{26} \\ C_{31} & C_{32} & C_{33} & C_{34} & C_{35} & C_{36} \\ C_{41} & C_{42} & C_{43} & C_{44} & C_{45} & C_{46} \\ C_{51} & C_{52} & C_{53} & C_{54} & C_{55} & C_{56} \\ C_{61} & C_{62} & C_{63} & C_{64} & C_{65} & C_{66} \end{bmatrix} \tag{4}$$

$C_{\alpha\beta}$ is a symmetric matrix that in the general case contains 21 different elements (triclinic symmetry), the worst case we can encounter in the rock structure. On the opposite end, the best

case is characterised by only 2 different elements (isotropic symmetry) where no anisotropic effect is present. A more complex case is defined by 9 different elements (orthorhombic symmetry), which can be found in shale or thin bedded sequences with vertical crack-sets. The best case that can be found in geophysical problem has 5 different elements (polar symmetry), corresponding to five independent elastic constants: V_P, V_S, the well-known Thomsen parameters ε and δ for V_P anisotropy and γ, the parameter for the V_s anisotropy:

$$V_P = \sqrt{\frac{C_{33}}{\rho}} \qquad V_S = \sqrt{\frac{C_{44}}{\rho}} \qquad \varepsilon = \frac{C_{11}-C_{33}}{2C_{33}} \qquad \delta = \frac{(C_{13}+C_{44})^2-(C_{33}-C_{44})^2}{2C_{33}(C_{33}-C_{44})} \qquad \gamma = \frac{C_{66}-C_{44}}{2C_{44}}. \tag{5}$$

This symmetry, generally present in shale or thin bedded sequences, is characterised by elastic properties that are different between the parallel and perpendicular directions with respect to an axis of symmetry, the so-called 'pole' (Fig. 1).

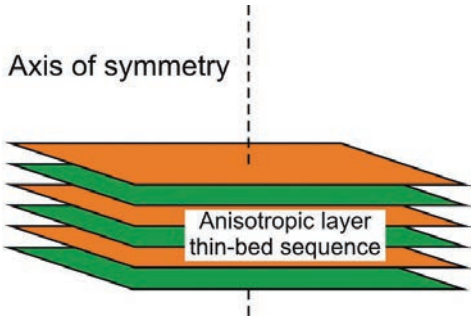

Fig. 1 - Polar symmetry.

In this study, as in most studies on seismic anisotropy, in order to reduce the complexity of the system, we consider the case of weak anisotropy, where the anisotropic parameters are estimated to be much lower than 1: $\varepsilon << 1$ (0.1-0.2), $\delta << 1$ (0.01-0.05), $\gamma << 1$ (0.1-0.2). Furthermore, we also included phase angle $\emptyset$ and group angle θ approximation (Thomsen, 1986; Kelter and Bancroft, 2004):

$$V_{SV}(\emptyset) = V_{SV}(\theta) \qquad V_{SH}(\emptyset) = V_{SH}(\theta). \tag{6}$$

In the case where the plane belonged to the vertical component and the axis of symmetry is orthogonal to the anisotropic layer and the ray direction is oblique to the layer (Fig. 2a), Thomsen's theory states that the velocity of the vertical and horizontal components of an S wave associated with a ray direction having an angle (θ) with respect to the axis of symmetry are defined as (Thomsen, 1986, 2002):

$$V_{SV}(\theta) \approx V_{S_\perp}\left[1 + \left(\frac{V_{P_\perp}}{V_{S_\perp}}\right)^2 (\varepsilon - \delta)\, sin^2\,\theta\, cos^2\theta\right] \quad V_{SH}(\theta) \approx V_{S_\perp}[1 + \gamma sin^2(\theta)] \tag{7}$$

where:

θ = angle of ray direction with axis of symmetry,

$$\gamma = \frac{Vs_{\parallel} - Vs_{\perp}}{Vs_{\perp}}, \tag{8}$$

ε, δ = Thomsen parameters,
$V_{P_\perp}$ = V_P velocity at vertical incidence ($\theta = 0$),
$V_{S_{||}}$ = V_S velocity parallel to the planes of anisotropy (maximum velocity component),
$V_{S_\perp}$ = V_S velocity perpendicular to the planes of anisotropy (minimum velocity component).

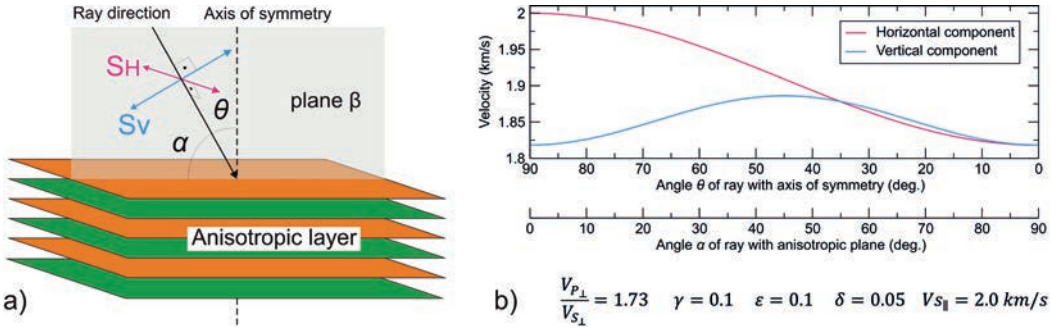

Fig. 2 - Geometric relationship between the S_V, S_H components and the anisotropic layer: a) case related to the theoretical formulas in Eq. 7; b) velocity values of the S_V, S_H components computed by applying formulas in Eq. 7 and referred to panel a.

If we consider a generic position of the anisotropic layers (Tilted Transverse Isotropy, TTI) with respect to the incident ray direction (Fig. 3), the S-wave components can be computed by a linear combination of the theoretical vertical and horizontal components $V_{SV}(\theta)$ and $V_{SH}(\theta)$, defined where the plane of the ray direction and the vertical component S_V is perpendicular to the anisotropic layer (plane β in Fig. 2a):

$$\left(V_{S_\perp}\right)_r = r_{V_\perp} V_{SV}(\theta) + r_{H_\perp} V_{SH}(\theta) \tag{9}$$

where:

$$r_{V_\perp} = \frac{VC_\perp}{VC_\perp + HC_\perp} \qquad r_{H_\perp} = \frac{HC_\perp}{VC_\perp + HC_\perp} \qquad VC_\perp = \cos\varphi_\perp \qquad HC_\perp = \sin\varphi_\perp \tag{10}$$

$$\left(V_{S_\parallel}\right)_r = r_{V_\parallel} V_{SV}(\theta) + r_{H_\parallel} V_{SH}(\theta) \tag{11}$$

where:

$$r_{V_\parallel} = \frac{VC_\parallel}{VC_\parallel + HC_\parallel} \qquad r_{H_\parallel} = \frac{HC_\parallel}{VC_\parallel + HC_\parallel} \qquad VC_\parallel = \cos\varphi_\parallel \qquad HC_\parallel = \sin\varphi_\parallel \tag{12}$$

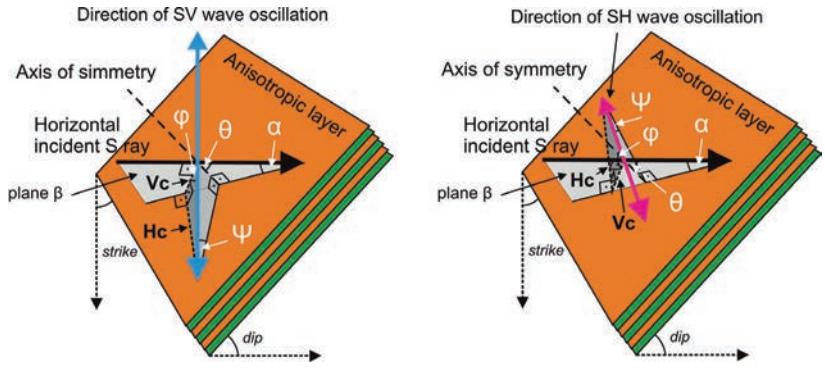

Fig. 3 - 3D schemes of the geometrical elements involved in the definition of Vc and Hc for the two directions of wave oscillation [vertical (a) and horizontal (b)]: horizontal incident S ray (black arrow); S_V and S_H direction of S-wave oscillation (blue and red arrows); Vc (vertical) and Hc (horizontal) components using to set the r_V and r_H constants in Eqs. 9 and 11 (black dashed segments). β is the plane orthogonal to the anisotropic layer and including the ray segment, which represents the reference plane to define the Vc and Hc components with respect to the direction of wave oscillation.

Fig. 4 shows the surfaces related to each component, $(V_{S_\perp})_r$ and $(V_{S_\parallel})_r$, computed by Eqs. 9 and 11, and referred to the dip and strike angles of the anisotropic plane for a horizontal incident ray, using:

$$\frac{V_{P\perp}}{V_{S\perp}} = 1.73 \quad \gamma = 0.1 \quad \varepsilon = 0.1 \quad \delta = 0.05 \quad Vs_{\parallel} = 2.0\ km/s \tag{13}$$

On the right of the same figure, the 2D plots of the two components are displayed, referred to the dip angle = 90° (above), and the strike angle = 0° (below), which correspond to the lower and right border, respectively, of the 3D representation shown on the left. These two plots show opposite trends of the two components: at dip angle = 90° V_{SV} is greater than V_{SH} for angles greater than 35° and reaches its maximum positive difference with respect to V_{SH} at strike angle = 90°; meanwhile at strike angle = 0° V_{SH} is greater than V_{SV} for angles less than 55° and reaches its maximum positive difference with respect to V_{SH} at dip angle = 0°.

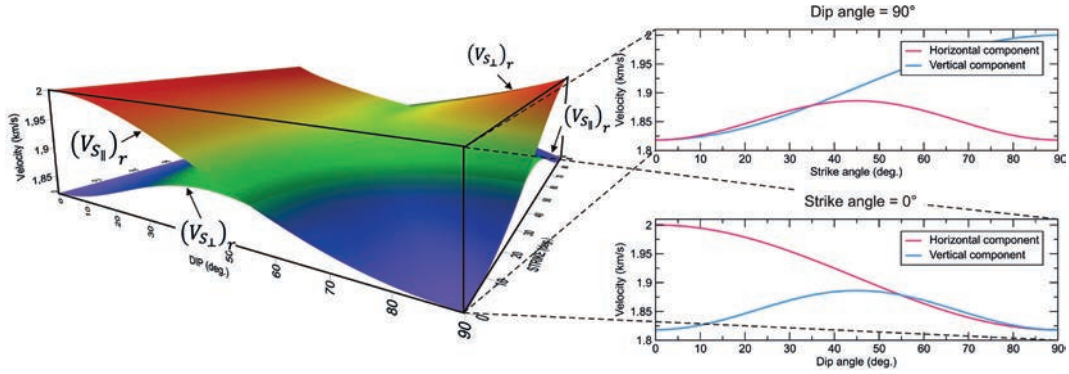

Fig. 4 - 3D display of the V_S components obtained from Eqs. 9 and 11, related to the dip and strike angles of the anisotropic layers and corresponding to a horizontal ray. On the right, the 2D plots corresponding to dip angle = 90° (above), and strike angle = 0° (below).

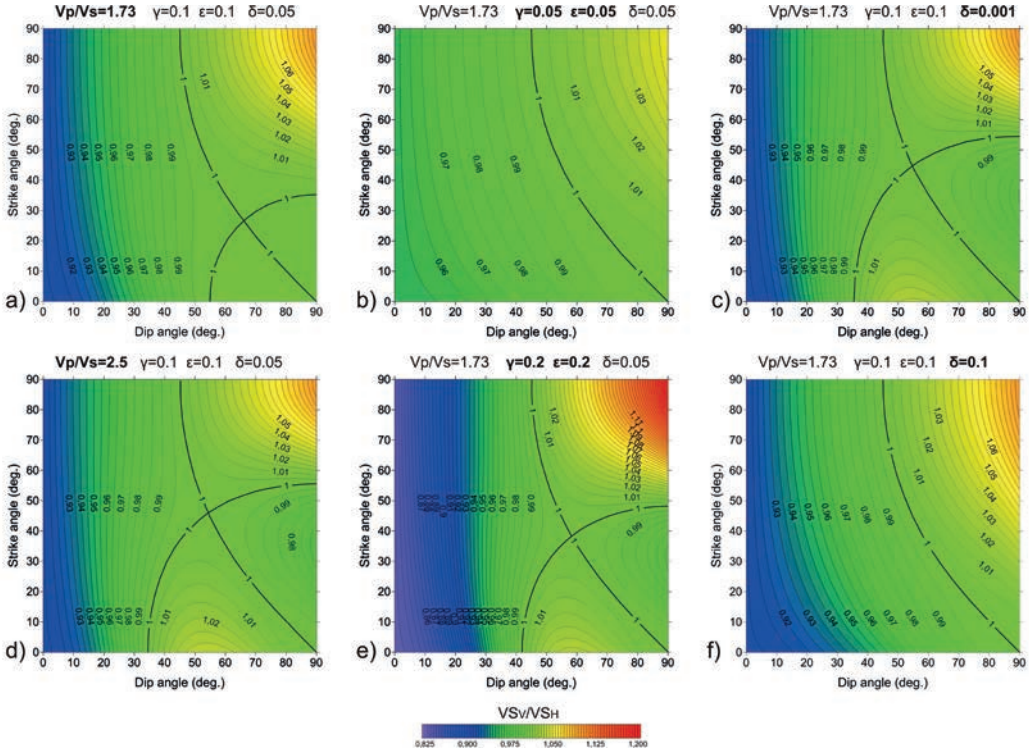

Fig. 5 - 2D maps of the V_{SV}/V_{SH} obtained by Eqs. 9 and 11 and corresponding to the 3D display of Fig. 4, using different values of V_P/V_S, γ, ε, and δ: a) and d) only changing V_P/V_S; b) and e) only changing γ and ε; c) and f) only changing δ. The bold isolines represents the V_{SV}/V_{SH} = 1.

To better understand the distribution and variation of the V_{SV}/V_{SH} values as the involved parameters (V_P/V_S, γ, ε, and δ) change, Fig. 5 displays some 2D maps of the V_{SV}/V_{SH} considering different values of these parameters. The maps are obtained by computing the single components using Eqs. 9 and 11. In all the displayed cases, the positive values of V_{SV}/V_{SH} are present in the areas corresponding to both high dip and strike angles; at the same time negative values correspond to low dip angles, while the strike angle ranges from 0° to 90°. The positive values of V_{SV}/V_{SH} appear also at lower strike angles and dip angles greater than 35-40° when V_P/V_S, and γ and ε are relatively high or in case of very low δ. Furthermore, it is evident that the N-S isoline corresponding to V_{SV}/V_{SH} = 1 never changes, independently of the values of the parameters.

The dip and strike angles versus V_{SV}/V_{SH} can also be displayed with respect to the angle of incidence a with the anisotropic plane (Fig. 6). In this figure, a 3D view highlights the intersections of the surfaces representing the dip and strike angles with different plane of constant V_{SV}/V_{SH} values. This representation, even if not easy to be interpreted, can be used to estimate a possible range of values of dip and strike angles, knowing the V_{SV}/V_{SH} from the result of the two tomographies.

3. Forward model: synthetic examples

As a further work, we implemented the S anisotropic case, based on Eqs. 9 and 11, in our already existing isotropic ray tracing code (Böhm *et al.*, 1999). It is based on the minimum time

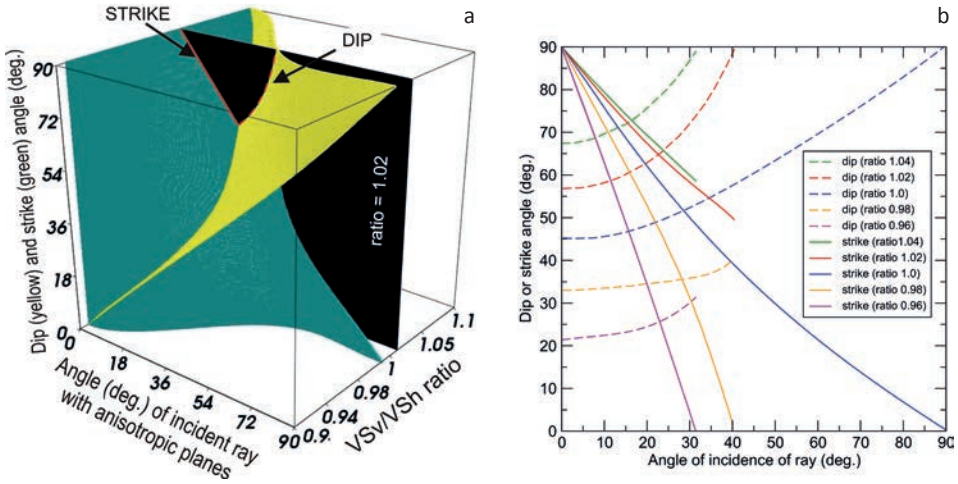

Fig. 6 - a) Display of the ratio of the components with respect to dip and strike angles and the angle of incidence of a horizontal ray with the anisotropic plane. In yellow the values related to dip angles, in green the values related to strike angles. The black plane corresponds to ratio 1.02. b) 2D plot of the intersections between the dip and strike curves at different V_{SV}/V_{SH} ratios. The red curves correspond to the red intersections in the 3D plot.

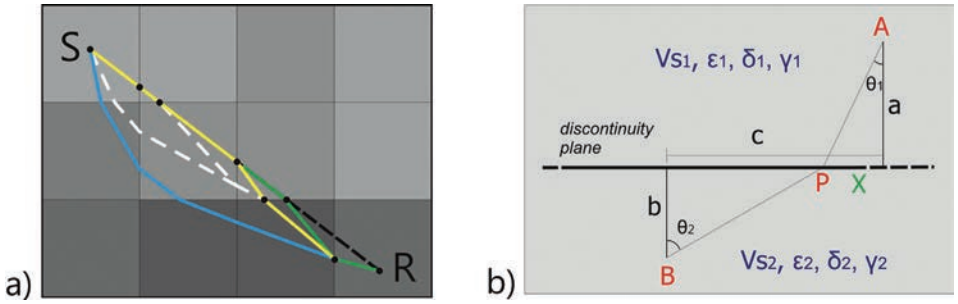

Fig. 7 - Description of the minimum time ray tracing algorithm used for the forward model computation in an irregular velocity grid. a) Ray path from source point (S) to receiver point (R): initial guess (black dashed line); first step of iterative process (green line); second step (yellow line); further steps (white dashed lines); final solution (blue line). Different gradations of grey correspond to different velocities. b) Scheme of the triplet position (APB) with respect to a discontinuity plane (i.e. border of pixel) referred to Eqs. 14 and 15 to compute the true position of point P (*x*-distance) according to the minimum time principle associated with the APB path.

approach, which uses an iterative method that applies Snell's law to each triplet of all the model intersections along the ray (Fig. 7a), until the ray path does not change significantly from the previous iteration. Inside each triplet, the correct 'Snell position' of point P is computed by zeroing the first derivative of the travel time function $F(x)$ between points A and B (Fig. 7b):

$$F(x) = \frac{\sqrt{a^2+x^2}}{Vs_1} + \frac{\sqrt{b^2+(c-x)^2}}{Vs_2} \tag{14}$$

$$F'(x) = [b^2 - (c-x)^2]x^2 - \frac{[Vs_1^2(c-x)^2(a^2+x^2)]}{Vs_2^2} = 0. \tag{15}$$

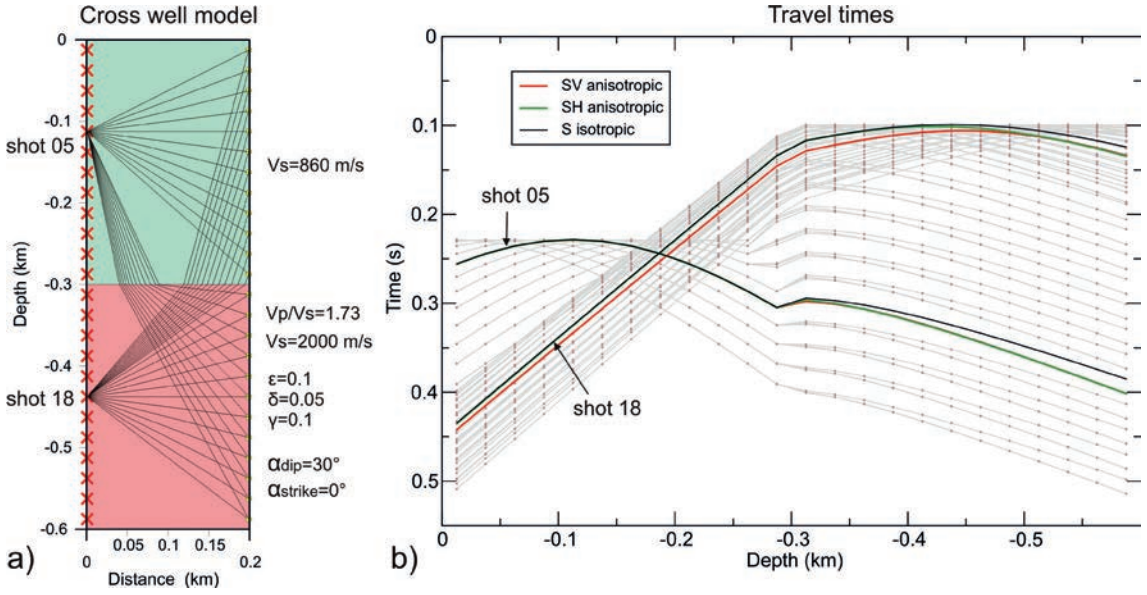

Fig. 8 - Cross-well synthetic example with an anisotropic area (red zone) in the lower part of the model: a) scheme of acquisition: 24 shots (red crosses) on the left, 24 receivers (yellow dots) on the right with rays from shot 05 (isotropic zone) and shot 18 (anisotropic zone); b) travel times computed from the cross-well acquisition in panel a.

In case of anisotropy, where ε, δ, and γ are defined in the model, a further iterative process is added inside each step of the main iterative sequence, and the point P is updated considering the direction of the ray segment involved in the anisotropic part, where Vs_1 and Vs_2 are defined by Eqs. 9 or 11.

Regarding the computation of different angles (α, θ, ψ, and φ) in Eqs. 9 and 11, the ray tracing algorithm uses the classical formulas of Cartesian geometry in the space.

Fig. 8 shows an example of travel time computation on a cross-well experiment. This case can also be considered equivalent to a seismic survey acquired on a horizontal plane between parallel tunnels in a mine environment. The used model presents an anisotropic layer in the lower part defined by:

$$\frac{V_{P\perp}}{V_{S\perp}} = 1.73 \quad \gamma = 0.1 \quad \varepsilon = 0.1 \quad \delta = 0.05 \quad Vs_{\parallel} = 2.0\ km/s \quad dip = 30° \quad strike = 0° \qquad (16)$$

Twenty-four shot points were placed on the left border and 24 receivers on the right border for a total of 576 travel times, displayed in Fig. 6b. In the same figure, two representative shots are shot 05, inside the isotropic part, and shot 18, inside the anisotropic part.

We also performed forward modelling for a seismic reflection case study (Fig. 9). We considered a three-layer model with a shallower isotropic layer (V_P = 1.5 km/s, V_S = 0.867 km/s) and a second anisotropic layer below (V_P = 3.460, V_{sII} = 2.0 km/s, $V_{S\perp}$ = 1.818 km/s, ε = 0.1, δ = 0.05, γ = 0.1). V_{sII} indicates the velocity parallel to the orientation of the anisotropic planes; while $V_{S\perp}$ indicates the velocity in the perpendicular direction. We defined three different orientations of the anisotropic planes inside the layer: model A, slightly dipping (30°), model B strongly dipping (70°), and model C, with dip = 70° and strike = 60°. We computed the travel times of the reflected arrivals from the second interface (the bottom of the anisotropic layer) for all the three models

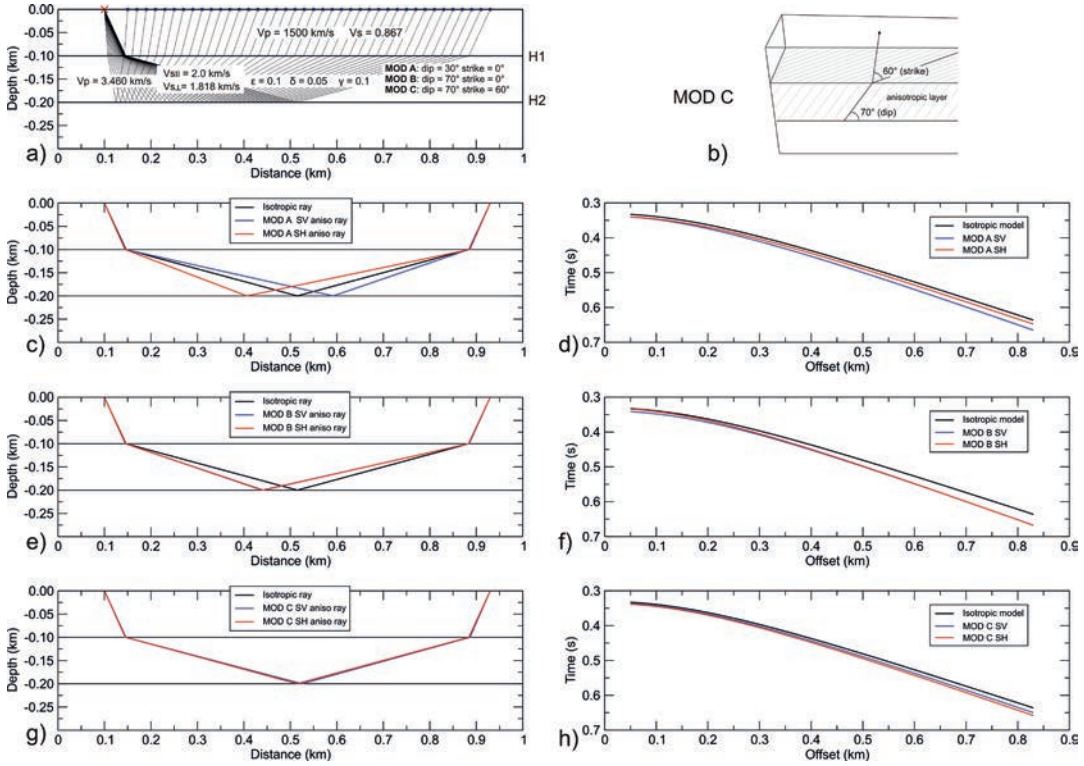

Fig. 9 - Travel times computation of reflected waves in a three-layers model with different anisotropic properties in the second layer: a) description of the models and scheme of the single-shot acquisition used for this experiment with the computed ray tracing; b) detail of the anisotropic layers orientation related to the model C; c), e), and g) different ray paths associated with the far offset for the three different cases: isotropic and anisotropic S_V and S_H arrivals; d), f) and h) the corresponding travel times related to panels c, e, and g.

(Fig. 9a). Figs. 9c to 9h show the rays and the corresponding travel times related to the largest offset and considering both the isotropic case (black rays) and the anisotropic cases relative to S_V (blue rays) and S_H waves (red rays). Model A (slightly dipping anisotropic planes) shows the greatest difference between the isotropic and anisotropic cases both for the ray paths and the travel times. In model B (strongly dipping anisotropic planes) the anisotropic ray paths are similar to each other but differ from the isotropic one. The last case (model C) shows a similar ray path for all the three cases, even if the travel times are different.

As a third example, we considered a synthetic case concerning the refracted (or diving) arrivals, which is typically used in near surface geophysical exploration and usually processed by first break tomography.

For this experiment we used a 2D model consisting of horizontal layers, with an anisotropic part below 50 m depth (Fig. 10a) defined by the same parameters of case A in the previous seismic reflection example ($\gamma = 0.1$, $\varepsilon = 0.1$, $\delta = 0.5$, dip = 30°, strike = 0°). The detailed S velocities used in this model are defined by the vertical function displayed on the right of Fig. 10a, where V_{SII} represents the fast component of S velocity, parallel to the horizontal orientation of the anisotropic layers. Using 25 shots, each spaced 20 m, along a set of 48 geophones, each spaced 10 m, we simulated the first arrivals for the fully isotropic S velocities and, considering the anisotropic part, for both vertical and horizontal S velocities components, by using Eqs. 9 and 11. Fig. 10b shows the first arrivals corresponding to these three cases and referred to a lateral shot.

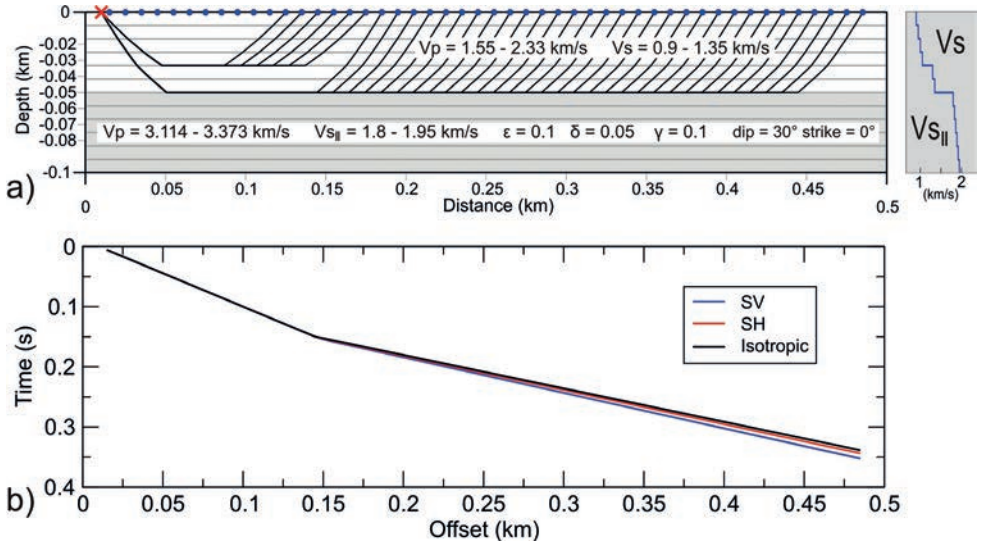

Fig. 10 - Synthetic example of first break arrivals on a horizontal layers model with anisotropic part below 50 m depth: a) details of the model parameters with the rays of the associated first arrivals of shot 01. On the right, the vertical profile of the S velocity, corresponding to the parallel direction of the anisotropic layers; b) first arrivals related to isotropic model and to vertical (S_V) and horizontal (S_H) S-wave components.

4. Anisotropy estimate: synthetic examples

In all the synthetic examples described in the previous chapter we used the travel time tomography to obtain the different S_V and S_H velocity fields from the inversion of the corresponding S_V and S_H arrivals, performed by the ray tracing on the true models. The computed values of the V_{SV}/V_{SH} ratio can be compared to the theoretical map of the V_{SV}/V_{SH} of Fig. 5 in order to estimate the possible scenarios of the anisotropic structures present in the investigated area.

In this work, the meaning of 'estimate' does not refer specifically to an inversion process, but is used to indicate a general evaluation of anisotropy, both for the orientation of the anisotropic layers and for the anisotropic parameters, starting from the V_{SV}/V_{SH} ratio, obtained by the travel time inversion of the S_V and S_H arrivals, and using the theoretical formulas (Eqs. 9 and 11).

The tomographic inversion was performed by the software package Cat3D, developed by OGS, which uses the ray tracing code described in the previous chapter and the Simultaneous Iterative Reconstruction Technique (SIRT) for the travel time inversion (Stewart, 1991). As a further improvement of the inversion we used the 'staggered grid' method (Vesnaver and Böhm, 2000), which enhances the model resolution (i.e. the model discretisation) without decreasing the reliability (i.e. increasing the null space, Böhm and Vesnaver, 1996) of the tomographic system. In all these experiments, the initial models, both in velocity and depth, can be quite different from the true ones. In fact, in these cases, they do not particularly affect the final result of the inversion, since we used acquisition geometries, and consequently rays path distribution, that provided well-posed tomographic systems, in terms of low null space.

Fig. 11 shows the results of the first example, relative to the cross-well case. The model was discretised by horizontal rectangular pixels corresponding to each source-receiver couple position at the same depth (Fig. 11a). The S_V and S_H velocities obtained only by the inversion of the arrivals associated with the horizontal rays (solid lines in Fig. 11b) allow us to better estimate the true V_{SV}/V_{SH} ratio (green line in Fig. 11c), as opposed to considering all the rays (black line in

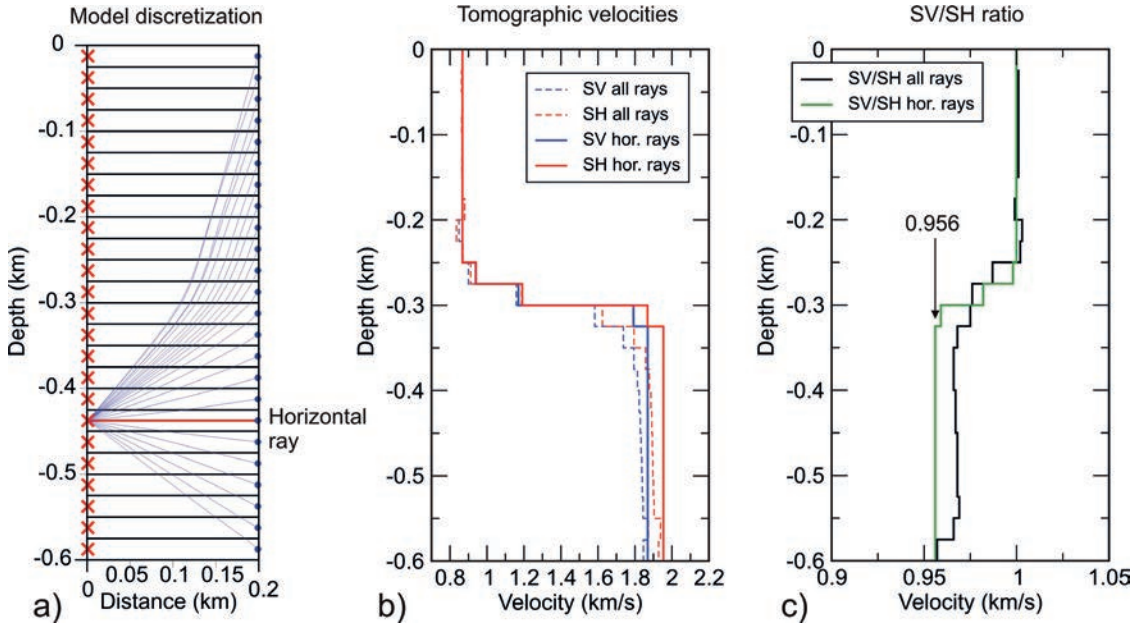

Fig. 11 - Anisotropic estimation related to cross-well synthetic example: a) model discretisation and ray tracing computed for shot 18, with in evidence the horizontal ray (red segment); b) tomographic velocities from all the travel times (dashed lines) and using only the travel times associated with the horizontal rays (solid lines) related to S_V arrivals (blue lines) and S_H arrivals (red lines); c) V_{SV}/V_{SH} ratio computed from the velocities using all the rays (black line) and only the horizontal rays (green line).

Fig. 11c). In fact, besides the border zone between isotropic and anisotropic areas, horizontal rays are less affected by the properties of the distant regions of the model. Fig. 11c shows two separate zones with different V_{SV}/V_{SH} values: 1 in the upper part of the model (isotropic) and 0.956 in the deeper part (anisotropic). These values correspond to the dip angle of 30° and strike angle of 0° in the map of Fig. 5a, defined by anisotropic parameters $V_P/V_S = 1.73$, $\gamma = 0.1$, $\varepsilon = 0.1$, $\delta = 0.5$. It is clear that usually we do not know the values of the anisotropic parameters only from the values of the V_{SV}/V_{SH} ratio. However, the values of this ratio can be considered useful additional information to better characterise the investigated area. For example, in this case, without knowing the anisotropic parameters, we can assume with some certainty that the dip of the anisotropic structure should be less than 30°-40° and most probably around 20°-30°.

Tomography was also applied to the second example of a reflection seismic experiment. In this case we used an iterative procedure that includes the SIRT algorithm for velocity estimation and the principle of minimum dispersion of reflection points (Carrion *et al.*, 1993) to detect the depth of each reflected interface; both applied in sequence at each step of the iterative process. The following steps were performed:

- get V_S of the first layer and the depth of the first interface from the inversion of the first reflected events, by applying the tomographic iterative procedure;
- get the V_{SV} and V_{SH} of the second layer and the depth of the second interface from the inversion of the corresponding S_V and S_H arrivals, keeping fixed the V_S of the first layer and the depth of the first interface.

Fig. 12 and Table 1 show the results of the inversion related to model A. The tomographic V_{SV} and V_{SH} obtained by this procedure (dashed lines) can be interpreted as an average value of the true anisotropic velocities associated with each segment of the rays that cross the second

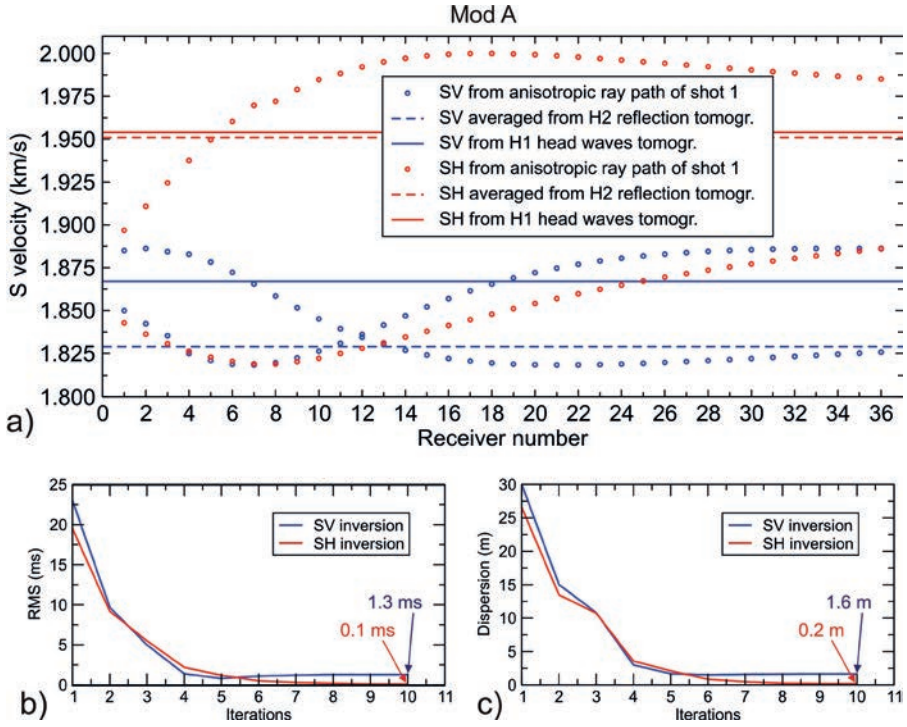

Fig. 12 - Anisotropic estimation related to reflection seismic experiment: a) dotted lines = S-wave velocity values computed in the two segments of ray crossing the second layer for each receivers of shot 1, associated with the S_V component (blue line) and S_H component (red lines) and considering the anisotropic parameters of model A (Fig. 9); dashed lines = S-wave velocities obtained from the travel time inversion of S_V (blue lines) and S_H (red lines) reflected arrivals from second horizon (H2); solid lines = S-wave velocities obtained from the travel time inversion of S_V (blue lines) and S_H (red lines) refracted arrivals (head waves) from the first horizon (H1); b) root-mean-square time residuals during the tomographic iterations of the S_V travel time inversion (blue line) and S_H travel time inversion (red lines); c) dispersion values computed for the H2 depth estimation in the reflected tomography related to S_V arrivals (blue line) and S_H arrivals (red lines).

layer (dotted lines). In fact, due to the unknown values of the anisotropic parameters γ, ε, and δ, tomography uses isotropic ray tracing. So, even if the V_{SV}/V_{SH} ratio (0.937) cannot be fully compared to the values of the maps of Fig. 5, which refer to horizontal direction of rays, it can give a rough indication of the orientation of the anisotropic layer. However, the true S_V and S_H velocities (solid line) associated with the horizontal rays can be easily obtained by the inversion of the arrivals identified as head waves from the first interface, by using the same procedure applied to the reflection tomography, provide that this kind of arrivals can be available and picked on the seismic data. Table 1 shows the high precision with respect to the true values (first column) of the S_V and S_H velocities (fourth and fifth columns) of the anisotropic layer, computed from the inversion of the head waves arrivals associated with the first interface.

The same results can be obtained in the case of a dipping anisotropic layer, by adding the inclination angle of the layer to the dip and strike angles estimated from the maps of Fig. 5.

Also in the third example (first break tomography) the anisotropic part of the investigated area can be recognised quite well from the V_{SV}/V_{SH} ratio (Fig. 13a). We cannot say the same for the estimation of the anisotropic parameters, due to the presence of several different segments of the rays crossing the anisotropic layer. Nevertheless, if we consider the lower part of the area illuminated by rays, which includes mostly sub horizontal rays, we can obtain a reliable estimate

Table 1 - Results concerning the synthetic example in the case of reflection seismic. The first column represents the true values of the model: the depth of the second interface, the V_S components of the anisotropic layer related to a horizontal ray and the corresponding V_{SV}/V_{SH} ratio. The second and third columns show the results of tomography from the reflected arrivals associated with the second interface. The fourth and fifth columns show the velocities obtained by tomography of the head waves arrivals from the first interface. The last row displays the values of the V_{SV}/V_{SH} ratio related to true values and to the two inversions.

	True value	**From S_V H2 reflection tomography**	**From S_H H2 reflection tomography**	**From S_V H1 head wave tomography**	**From S_H H1 head wave tomography**
Depth of the 2nd interface	0.2 km	-0.198 km	-0.205 km		
V_{SV} on horizontal ray	1.869 km/s	1.829 km/s		1.867 km/s	
V_{SH} on horizontal ray	1.954 km/s		1.951 km/s		1.954 km/s
V_{SV}/V_{SH}	0.956	0.937		0.955	

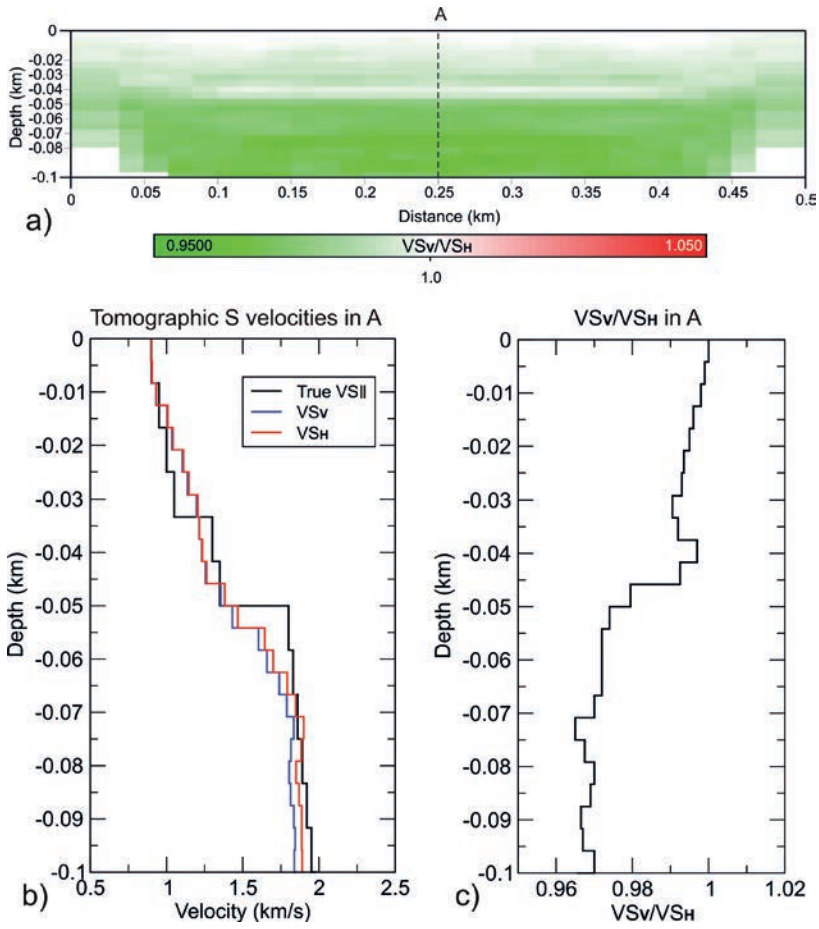

Fig. 13 - Anisotropic estimation related to the third synthetic case (first break tomography): a) vertical section of the V_{SV}/V_{SH} distribution obtained from the separate travel time inversions of S_V and S_H first break arrivals; b) vertical functions of tomographic S_V (blue) and S_H (red) velocities compared with the true V_S parallel component to the anisotropic layer (black line), extracted in point A; c) V_{SV}/V_{SH} ratio computed with the same velocities displayed in panel b.

of the orientation of the anisotropic structure from the maps of Fig. 5. The smoothed velocity values observed in the vertical function of Fig. 13b (blue and red lines), with respect to the true values (black line), are due to an intrinsic property of the inversion algorithm (SIRT) and in particular when using first break tomography.

The choice of starting velocity model for tomography was not a crucial aspect in the two first cases, since the distribution of rays allows the inversion algorithm to reach the same final solution using different starting models, even far from the true values. Instead, the third case is more critical about this choice, because the existence of diving ray paths assumes the presence of a positive velocity vertical gradient. In this case, we defined the starting model with a linear velocity vertical gradient obtained by a smoothed velocity field computed from the inversion of the same travel times but using non-bent diving ray paths and fixed the depth of the arc as 0.2 the offset distance. In the case of real data, we can use, if they exist, well data, the geology of the area or results from a closing survey to define the starting velocity model.

As a final consideration, in all these cases we can add precious information about the P-wave anisotropic parameters ε and δ, which can be obtained by different methods developed in the last decades [one of these (Böhm, 2018) uses the tomographic approach in a similar way to this work], in order to constrain ε and δ parameters and better estimate the orientation (dip and strike) of the anisotropic structures from the maps of Fig. 5.

5. Anisotropy estimate: real case

It is clear that univocal information on the orientation (dip and strike) of an anisotropic structure only from the V_{SV}/V_{SH} ratio cannot be obtained. However, if we consider the information derived from the ray segments, which can be known from the ray-based tomography, and taking into account some assumptions, constraints, or geological information, we can achieve a realistic estimate of the anisotropic parameters and of the geometries of the buried anisotropic structures from the V_{SV} and V_{SH} velocity fields, obtained by the tomographic inversion of the corresponding arrivals.

This approach was applied in a real experiment where both S_V and S_H arrivals were acquired in a high-resolution seismic line.

Seismic acquisition of S waves was performed twice by using 10-Hz single horizontal geophones and an S-wave seismic vibrator. The first time the geophones and the vibrator were oriented in-line to the direction of the seismic line; the second time the geophones and the vibrator were oriented cross-line to the direction of the seismic line. A complete description of this survey can be found in Da Col *et al.* (2021). In both data sets, the first S arrivals were picked and inverted by using the ray-based tomography with SIRT algorithm and applying the 'staggered grid' method, as described in the synthetic experiments. The picking of the first arrivals was not easy in both data sets. For this reason we used the S first arrivals computed on the V_S model obtained from the V_P model, converted using $V_P/V_S = 1.73$, a ratio generally found in rocks, as a guide to interpret and recognise the effective S arrivals to be picked (Fig. 14). A smoothed version of this V_S model was also used as a starting model for the inversion of the picked S first arrivals. The root-mean-square of time residuals (difference between the observed and computed times) of inversion was 2.1 ms (3.8 in percentage with respect to the observed times) and 1.1 (3.5%) respectively for S_V and S_H data. Fig. 15 shows the results of the two velocity fields, S_V (Fig. 15a) and S_H (Fig. 15b), obtained by first-break tomography, and the map of the S_V/S_H distribution in the same area (Fig. 15c). In general, large differences between V_{SV} and V_{SH} can be related to

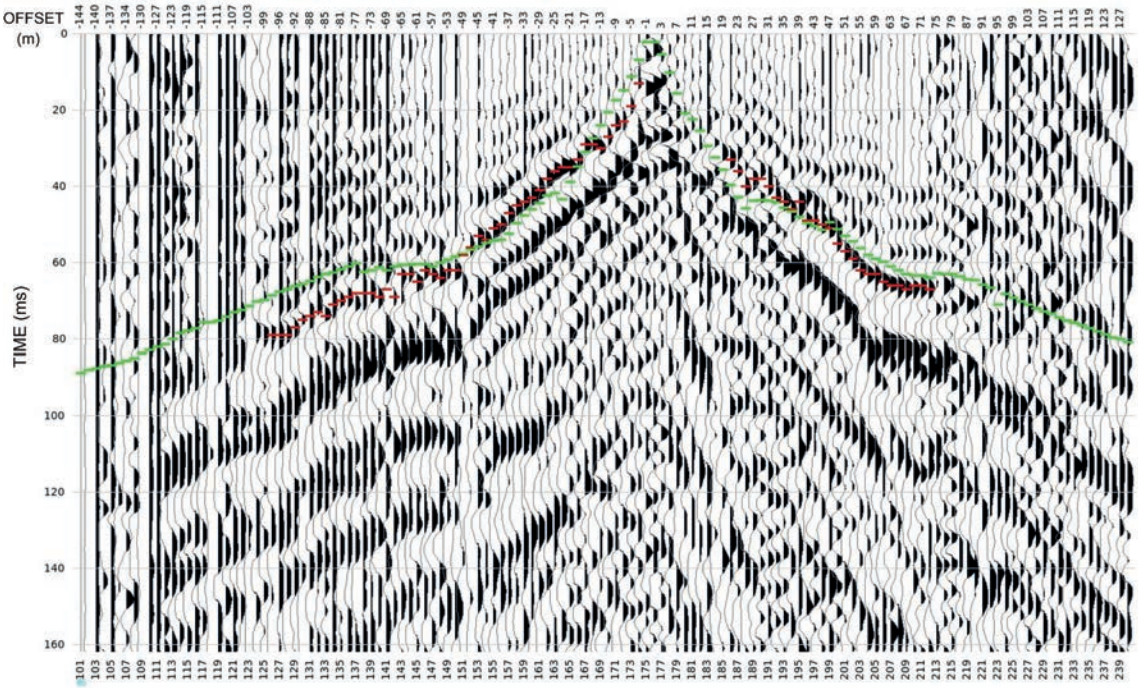

Fig. 14 - Example of common shot gather of S_H data. In green, the arrivals from the V_S model, converted from P velocities (from V_P/V_S = 1.73) and used as guide to pick the SH first break (red) for the travel time inversion.

the presence of anisotropic structures. This figure and the corresponding cross-plot of the two parameters involved (V_{SH} vs. V_{SV}), highlights a prevailing ratio value greater than one, in particular for the deeper parts of the investigated area.

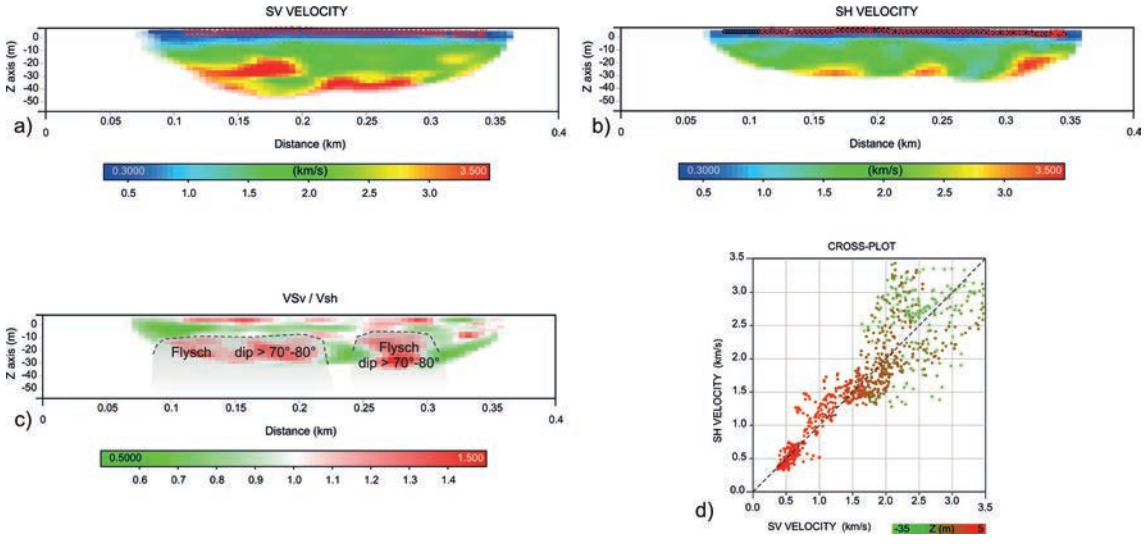

Fig. 15 - Travel time tomography of first arrivals from S_V (a) and S_H (b) real data; c) the computed V_{SV}/V_{SH} ratio with the interpreted position of the flysch block (grey areas) corresponding to high values of V_{SV}/V_{SH}; d) cross-plot of V_{SH} vs. V_{SV}; the dashed line indicates ratio = 1.

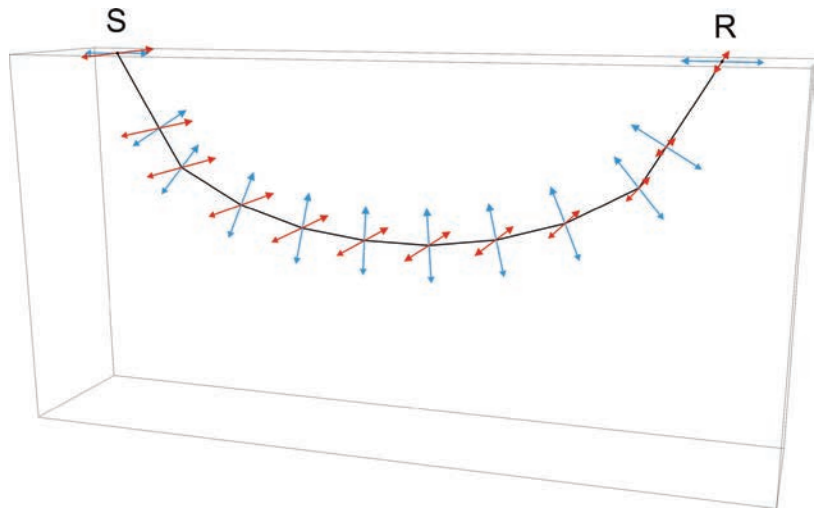

Fig. 16 - Scheme of a ray path associated with a diving wave, used in turning ray tomography applied to the first arrivals. Red arrows indicate the particle motion of the horizontal component (S_H) of the S waves. Blue arrows indicate the particle motion of the vertical component (S_V) of the S waves.

From the geologic information (Buljan *et al.*, 2006), the study area is characterised by a Cenozoic/Eocene flysch covered by Quaternary sediments. The dominant larger S_V than S_H velocities can be a reliable indicator of the geometry of the anisotropic structures. In fact, under the hypothesis of weak anisotropy, following the 2D maps of Fig. 5, and considering the prevalent horizontal direction of the diving ray paths involved in the deeper part of the investigated area (Fig. 16), we can presume two possible scenarios for the orientation and dip of the buried structures. In the first one, related to high anisotropy (e and g) and V_P/V_S values (Figs. 5d, 5e), we can estimate dip angles of the anisotropic layers (flysch) between 50 and 80°, while the strike direction shows very low angles (< 10°). In the second scenario, high V_{SV}/V_{SH} values correspond to both dip and strike angles greater than 50-60° and, since this ratio is generally greater than 1.1, we can also induce high values of ε and γ (Fig. 5e). However, because the geological map of this area, published in Buljan *et al.* (2006), shows a prevalent E-W strike direction similar to that of the seismic line considered in this work, with an associated dip angle greater than 70-80°, we consider the second scenario more realistic for this area. Regarding the source of anisotropy, we have no element to distinguish layering or fracturing in the flysch.

Whenever processing real data, we must take into account an important part concerning uncertainties and ambiguities due to various aspects of inversion. In particular the errors introduced by the human interpretation and capacity to elaborate the data (picking and choice of the processing parameters), inaccuracy of the used codes (ray tracing and inversion algorithms), and intrinsic errors in the instrumental parts (sources and geophones). The reliability of the inversion is another important aspect to be considered, which is generally caused by how the tomographic system (acquisition geometry, i.e. ray distribution, and model discretisation) is posed with respect to the inversion. Ray coverage, time residuals analysis and null space map can be useful tools to measure this property of the inversion. It is clear that also the estimate of anisotropy is affected by all these uncertainties of the inversion.

Due to the complexity of this aspect, generally, it is not possible to quantify the errors that we introduce in the inversion process. So, in some cases, it is better to evaluate and interpret the results of the tomography by considering the qualitative viewpoint prevalent.

6. Conclusions

We proposed a new method to estimate the anisotropy from the velocities of the S_V and the S_H wavefields. Such method is based on a geometrical approach to compute the S- velocity components that use the ray paths derived from the travel times tomography. Specifically, we exploit the ratio of S_V/S_H velocity fields to estimate the orientation of the anisotropic layer (strike and dip angles) using the relationship among the V_{SV}/V_{SH} ratio, the ray segment direction, and the magnitude of the anisotropy (γ, ε, and δ).

From this analysis, we conclude that, even though we cannot acquire unique information about the orientation (dip and strike) of an anisotropic structure only from the V_{SV}/V_{SH} ratio, we can obtain useful information about the structure of the anisotropic layer by using the ray segments obtained from ray-based tomography, as well as considering some assumptions, constraints, or geological knowledge.

Acknowledgments. The real data presented in this paper were acquired in the frame of the PMO-GATE (Preventing, Managing and Overcoming Natural-Hazards Risks to mitiGATE economic and social impact) project, which is EU co-funded in the Italy-Croatia Interreg programme. The authors thank our colleague Fabio Cavallini for the precious contribution to the ray tracing code.

REFERENCES

Bale R.A., Gratacos B., Mattocks B., Roche S., Poplavskii K. and Li X.; 2009: *Shear wave splitting applications for fracture analysis and improved imaging: some onshore examples*. First Break, 27, 73-83, doi: 10.1190/1.9781560803362.appk.

Beecherl J. and Hardage B.A.; 2004: *Shear wave seismic study comparing 9C3D SV and SH images with 3C3D C-Wave images.* Office of Scientific and Technical Information, UNT Digital Library, Final technical report, #834140, 71 pp., doi: 10.2172/834140.

Böhm G.; 2018: *Estimation of anisotropy parameters in VTI media using the Ray-Based Tomography.* In: Expanded Abstracts 24th European Meeting of Environmental and Engineering Geophysics, Near Surface Geoscience 2018, Porto, Portugal, 5 pp., doi: 10.3997/2214-4609.201802506.

Böhm G. and Vesnaver A.; 1996: *Relying on a grid.* J. Seismic Explor., 5, 169-184.

Böhm G., Rossi G. and Vesnaver A.; 1999: *Minimum time ray-tracing for 3-D irregular grids*. J. Seismic Explor., 8, 117-131.

Buljan R., Pollak D. and Pest D.; 2006: *Engineering geological properties of the rock mass along the Kastela bay sewage system*. In: Proc. 10th International Symposium IAEG, Geological Society of London, Nottimgham, UK, pp. 467-477.

Carrion P., Böhm G., Marchetti A., Pettenati F. and Vesnaver A.; 1993: *Reconstruction of lateral gradients from reflection tomography.* J. Seismic Explor., 2, 55-67.

Chmiel M. and Bardainne T.; 2014: *Tomography of a velocity model and location of microseismic events with P, SV and SH waves.* In: Proc. 76th EAGE Conference and Exhibition 2014, Amsterdam, The Netherlands, pp. 492-496, doi: 10.3997/2214-4609.20141437.

Da Col F., Accaino F., Böhm G. and Meneghini F.; 2021: *Characterisation of shallow sediments by processing of P, SH and SV wavefields in Kaštela (HR).* Eng. Geol., 293, 106336, doi: 10.1016/j.enggeo.2021.106336.

Fishman K.L. and Ahmad S.; 1995: *Seismic response for alluvial valleys subjected to SH, P, and SV waves*. Soil Dyn. Earthquake Eng., 14, 249-258.

Kelter A.C. and Bancroft J.C.; 2004: *Characteristics of P, SV, SH wave propagation in an anisotropic medium.* CREWES Res. Report, 16, 1-31.

Leary P.C., Li Y.G. and Aki K.; 1987: *Observation and modelling of fault-zone fracture seismic anisotropy - I. P, SV and SH travel times*. Geophys. J. Int., 91, 461-484, doi: 10.1111/j.1365-246X.1987.tb05239.x.

Love A.E.H.; 1927: *A treatise on the mathematical theory of elasticity 4 ed.* Cambridge University Press, Cambridge, UK, 662 pp.

Macrides C.G. and Kelamis G.; 2000: *A 9-C, 2-D land seismic experiment for lithology estimation of a Permian clastic reservoir.* The Leading Edge, 19, 1109-1116, doi: 10.1190/1.1438488.

Musgrave M.J.P.; 1970: *Crystal acoustics: introduction to the study of elastic waves and vibrations in crystals.* Holden-Day, San Francisco, CA, USA, 303 pp.

Stewart R.R.; 1991: *Exploration seismic tomography: fundamentals.* Society of Exploration Geophysicists, Course note series, vol. 3, 190 pp., doi: 10.1190/1.9781560802372.

Suroso T., Laksono H., Triyoso W. and Priyono A.; 2017: *Estimating anisotropy parameter by shear wave splitting of crosswell seismic data: a case study on inter-bedded sand-shale layers*. In: Proc. Southeast Asian Conference on Geophysics (SEACG 2016), IOP Conference Series Earth and Environmental Science, Bali, Indonesia, Vol. 62, 012019, doi: 10.1088/1755-1315/62/1/012019.

Thomsen L.; 1986: *Weak elastic anisotropy*. Geophys., 51, 1954-1966, doi: 10.1190/1.1442051.

Thomsen L.; 2002: *Understanding seismic anisotropy in exploration and exploitation*. Society of Exploration Geophysicists and The European Association of Geoscientists and Engineers, 2002 Distinguished Instructor Short Course, Series 5, 253 pp., doi: 10.1190/1.9781560801986.ch4.

Vesnaver A. and Böhm G.; 2000: *Staggered or adapted grids for seismic tomography?* The Leading Edge, 19, 944-950, doi: 10.1190/1.1438762.

Wang B. and Zhang F.; 2021: *Inversion of SH-SH wave anisotropy parameter in VTI media*. In: Proc. 82nd EAGE Annual Conference and Exhibition 2021, Amsterdam, The Netherlands, 5 pp., doi: 10.3997/2214-4609.202113256.

Corresponding author: Gualtiero Böhm
Istituto Nazionale di Oceanografia e di Geofisica Sperimentale - OGS
Borgo Grotta Gigante - Sgonico - Italy
Phone: +39 339 2441458, e-mail: gbohm@ogs.it